

For the origin of the anomalous negative TMR effect, the TMR ratio can be formulated in terms of the spin polarizations of electrodes (i.e., the difference between the DOS of up and down spin bands). According to Julliere's formulation (24), the TMR ratio at a low bias-voltage limit is expressed as

$$\text{TMR} = (R_a - R_p)/R_p = 2PP'/(1 - PP') \quad (1)$$

where P and P' are the spin polarizations of the two electrodes. Because the spin polarization of Ni-Fe is positive (25), the negative TMR indicates that the spin polarization of the Co-Cu electrode is effectively switched by the resonant-tunneling effect. Standing waves of wave functions of the conduction electrons (i.e., the QW states) in Cu(001) are effectively formed under the condition $t_{\text{Cu}} \cdot q + \alpha_1 + \alpha_2 = 2\pi n$, where α_1 and α_2 are phase changes of the electron wave functions induced by the reflections at the Co-Cu and Cu-Al-O interfaces, respectively, and n is an integer number. The QW states are formed when $t_{\text{Cu}} = 2\pi n/q_1 + \text{constant}$; therefore, the period of QW oscillation is $2\pi/q_1$. Because the down-spin electrons are mainly confined in the Cu layer, the QW states should have a negative spin polarization. Thus, the TMR effect may change sign with a periodicity of $2\pi/q_1 \approx 11 \text{ \AA}$.

The TMR oscillation at various bias voltages is shown in Fig. 4A. All the curves can be fitted by using the same damped oscillation function. The parameters (e.g., the oscillation period, phase, and amplitude) change depending on the bias voltage. Here we discuss only the oscillation period, whose physical origin is the most straightforward. Figure 4B shows the bias dependence of the oscillation period. Under a positive bias, the oscillation period increases with the bias voltage. Under a negative bias, on the other hand, the oscillation period is approximately independent of the bias voltage. The theoretical value of the oscillation period estimated from the band structure of Cu (26) is also shown in Fig. 4B. The overall shape of the observed bias dependence is well reproduced by the theoretical estimation. To obtain the theoretical curve, we assumed a simple picture in which ballistic electrons tunnel from one electrode into the other without energy loss (Fig. 4C). Under a positive bias ($+V$), electrons at the Fermi level (E_F) in Ni-Fe dominantly tunnel into the empty states at $E_F + eV$ in Cu. In this case, the QW states at $E_F + eV$ in Cu have a strong influence on the TMR effect. Therefore, the oscillation period is determined by the length of the \mathbf{q}_1 vector at $E_F + eV$. Thus, the period is expected to depend on the bias voltage, reflecting the energy dependence of q_1 (i.e., the energy dispersion of the Δ_1 band of Cu along the Γ -X axis) (Fig. 4D) (26). Under a negative bias ($-V$), on the other hand, electrons at E_F in Cu dominantly tunnel into the empty

states at $E_F + eV$ in Ni-Fe. In this case, the QW states at E_F in Cu have a strong influence on the TMR effect. Therefore, the oscillation period is expected to be independent of the bias voltage. The observed period at zero bias is slightly longer than the theoretical value. This discrepancy is also observed in the interlayer exchange coupling, where the observed oscillation period (27) is usually longer than the theoretical estimation (21). Although the theoretical estimation is based on an assumption that the tunneling process is ballistic (without energy loss), the observed TMR oscillation can be well explained by the theory.

We have shown that the coherence of spin-polarized tunneling electrons can be conserved after multiple reflections in the electrode, resulting in the spin-polarized resonant tunneling. With the use of this effect, it is possible to develop highly functional spin-electronic devices based on coherent transport, such as the resonant-tunneling spin transistor and quantum information devices.

References and Notes

1. G. A. Prinz, *Science* **282**, 1660 (1998).
2. S. A. Wolf et al., *Science* **294**, 1488 (2001).
3. J. S. Moodera, L. R. Kinder, T. M. Wong, R. Meservey, *Phys. Rev. Lett.* **74**, 3273 (1995).
4. T. Miyazaki, N. Tezuka, *J. Magn. Magn. Mater.* **139**, L231 (1995).
5. J. M. de Teresa et al., *Science* **286**, 507 (1999).
6. L. Esaki, *IEEE J. Quantum Electron.* **22**, 1611 (1986).

7. X. Zhan, B. Li, G. Sun, F. Pu, *Phys. Rev. B* **56**, 5484 (1997).
8. J. E. Ortega, F. J. Himpsel, G. J. Mankey, R. F. Willis, *Phys. Rev. B* **47**, 1540 (1993).
9. Y. Suzuki et al., *Phys. Rev. Lett.* **80**, 5200 (1998).
10. A. Vedyayev, N. Ryzhanova, C. Lacroix, L. Giacomoni, B. Dieny, *Europhys. Lett.* **39**, 219 (1997).
11. J. Mathon, A. Umerski, *Phys. Rev. B* **60**, 1117 (1999).
12. J. J. Sun, P. P. Freitas, *J. Appl. Phys.* **85**, 5264 (1999).
13. J. S. Moodera et al., *Phys. Rev. Lett.* **83**, 3029 (1999).
14. P. LeClair, H. J. M. Swagten, J. T. Kohlhepp, R. J. M. van de Veedonk, W. J. M. de Jonge, *Phys. Rev. Lett.* **84**, 2933 (2000).
15. J. S. Moodera, T. H. Kim, C. Tanaka, C. H. de Groot, *Philos. Mag.* **80**, 195 (2000).
16. P. LeClair, J. T. Kohlhepp, H. J. M. Swagten, W. J. M. de Jonge, *Phys. Rev. Lett.* **86**, 1066 (2001).
17. P. LeClair et al., *Phys. Rev. B* **64**, 100406-1 (2001).
18. T. Nagahama, S. Yuasa, Y. Suzuki, E. Tamura, *Appl. Phys. Lett.* **79**, 4381 (2001).
19. S. Yuasa et al., *Europhys. Lett.* **52**, 344 (2000).
20. See supporting data on Science Online.
21. P. Bruno, C. Chappert, *Phys. Rev. Lett.* **67**, 1602 (1991).
22. A. Cebollada et al., *Phys. Rev. B* **39**, 9726 (1989).
23. C. B. Duke, *Tunneling in Solids* (Academic Press, New York, 1969), chap. IV.
24. M. Julliere, *Phys. Lett.* **54A**, 225 (1975).
25. R. Meservey, P. M. Tedrow, *Phys. Rep.* **238**, 173 (1994).
26. B. Segall, *Phys. Rev.* **125**, 109 (1962).
27. W. Weber, R. Allenspach, A. Bischof, *Europhys. Lett.* **31**, 491 (1995).

Supporting Online Material

www.sciencemag.org/cgi/content/full/297/5579/234/DC1
Materials and Methods
Fig. S1

26 February 2002; accepted 13 May 2002

Spontaneous Organization of Single CdTe Nanoparticles into Luminescent Nanowires

Zhiyong Tang,¹ Nicholas A. Kotov,^{1*} Michael Giersig²

Nanoparticles of CdTe were found to spontaneously reorganize into crystalline nanowires upon controlled removal of the protective shell of organic stabilizer. The intermediate step in the nanowire formation was found to be pearl-necklace aggregates. Strong dipole-dipole interaction is believed to be the driving force of nanoparticle self-organization. The linear aggregates subsequently recrystallized into nanowires whose diameter was determined by the diameter of the nanoparticles. The produced nanowires have high aspect ratio, uniformity, and optical activity. These findings demonstrate the collective behavior of nanoparticles as well as a convenient, simple technique for production of one-dimensional semiconductor colloids suitable for subsequent processing into quantum-confined superstructures, materials, and devices.

Unique structure and optical and electrical properties of one-dimensional (1D) semiconductors and metals make them the key structural blocks for a new generation of electron-

ics, sensors, and photonics materials. Several synthetic methods of nanowire and nanorod production have been developed (1-8), but they all are based on point-initiated uniaxial growth of the crystal. Lateral expansion of the crystal lattice is arrested by a rigid template or by unfavorable kinetics. We describe a method of nanowire synthesis based on a different principle—a crystalline nanowire spontaneously self-assembles from individual nanoparticles. This technique of nanowire

¹Chemistry Department, Oklahoma State University, Stillwater, OK 74078, USA. ²Hahn-Meitner-Institut, Abteilung Physikalische Chemie Glienickestrasse 100, D-15109, Berlin, Germany.

*To whom correspondence should be addressed. E-mail: kotov@okstate.edu

synthesis is simple, and the quality and optical activity of the nanowires either surpasses or is comparable to 1D species produced by more laborious processes.

CdTe nanocrystals of different diameters stabilized by thioglycolic acid were prepared as described elsewhere (9, 10). One of the key steps in the preparation of nanowires from nanoparticles was the removal of excess stabilizer. To accomplish that, CdTe colloids were precipitated by methanol addition and were redissolved in pure water at pH 9.0, which resulted in the partial removal of the stabilizer. The obtained dispersion was allowed to age in darkness at room temperature for several days. During this period, the color of the solution gradually became darker, and the quantities of nanowires and their lengths, as observed by transmission electron microscopy (TEM) and tapping atomic force microscopy (AFM), gradually increased. The process of nanowire growth continued over a period of 7 days.

Four different CdTe dispersions with luminescence maxima at 520 to 530 (green), 550 to 565 (yellow), 590 to 605 (orange), and 610 to 625 (red) nm were used for the preparation of nanowires (Fig. 1). As expected (11), the nanowire growth was accompanied by the red shift of the luminescence peaks of the dispersion, which reached its maximum of 10 to 20 nm in 7 days (Fig. 1). The red shift occurs due to the decrease of confinement in one dimension.

Figure 2 shows the TEM and AFM images of the typical nanowires synthesized from CdTe dots of different diameters. All images are representative in terms of the level of perfection and physical parameters of the nanowires that can be routinely achieved. The cumulative characteristics for a variety of nanowires obtained in TEM and AFM studies are given in Table 1. All the prepared nanowires had a narrow standard deviation of their diameters $\delta = 5$ to 15% and aspect ratios as high as 500 (Fig. 2, A and C). An important observation can be made on the basis of the data presented in Table 1: the diameters of the nanowires

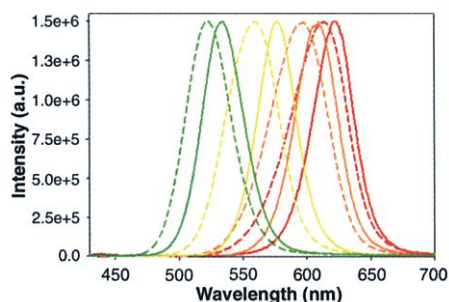


Fig. 1. Luminescence spectra of parent CdTe nanoparticles (dashed lines) and resulting nanowires (solid lines) marked by the corresponding luminescence colors.

are virtually identical to the diameters of precursor nanoparticles.

High-resolution TEM (Fig. 3, A and B) shows that the produced nanowires are single-crystalline in structure, albeit with some defects. Lattice plane spacings calculated from the diffraction patterns are 3.98 Å hkl (100) and 2.29 Å hkl (110) and are typical for hexagonal wurtzite CdTe structures. As shown by vector diagrams in Fig. 3, the perpendicular orientation of the (100) planes in respect to the nanowire axis and slanted (110) plane projection indicate that the long axis of nanowire is parallel to the (001) direction of wurtzite crystal lattice. This orientation is maintained for all nanowires pro-

duced, regardless of the initial particle size.

CdTe nanocrystals have cubic zinc blend structure (9), and, therefore, the nanowire growth is accompanied by a phase transition. This occurs because the hexagonal lattice is intrinsically anisotropic and has a unique (001) axis (6). CdTe nanocrystals reorganize their lattice to obtain the match between the symmetry of the crystal and the uniaxial geometry of 1D species. This process is facilitated by the low activation energy of phase transition of CdTe (12) and by the partial removal of the stabilizer coating.

To reveal the intermediate steps in the nanoparticle to nanowire transition, the aliquots of the dispersions in the early stages of

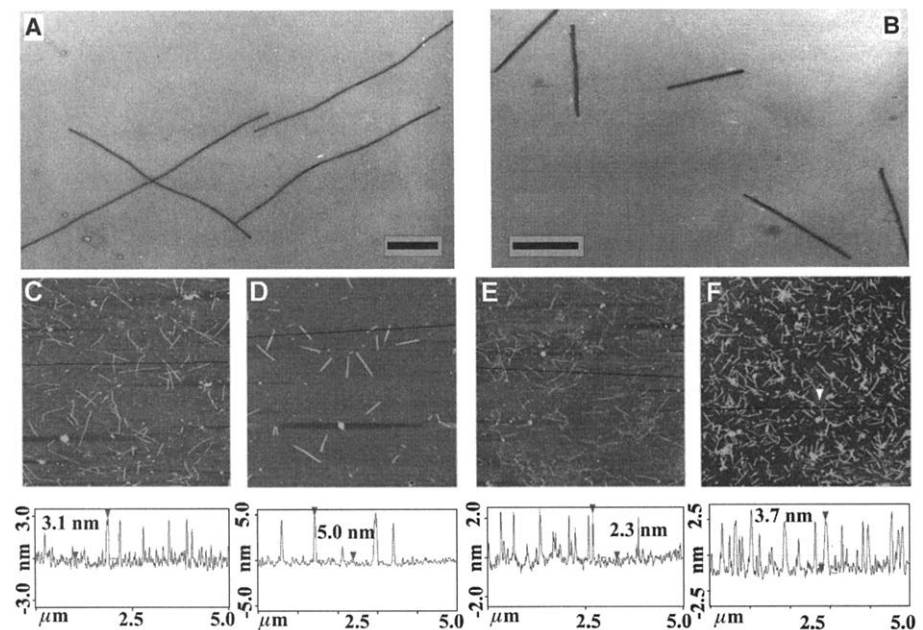


Fig. 2. TEM images of CdTe nanowires made from 3.4- (A) and 5.4-nm (B) nanoparticles. Bars, 100 nm. AFM images (top) and cross-sectional profiles (bottom) of nanowires made from 3.4- (C), 5.4- (D), 2.5- (E), and 4.1-nm (F) CdTe dots. A featureless cationic polyelectrolyte layer [poly(diallyldimethylammonium)chloride], with surface features of 0.1 nm in height, was preadsorbed on the silica wafer to increase the adhesion of anionic nanowires (22).

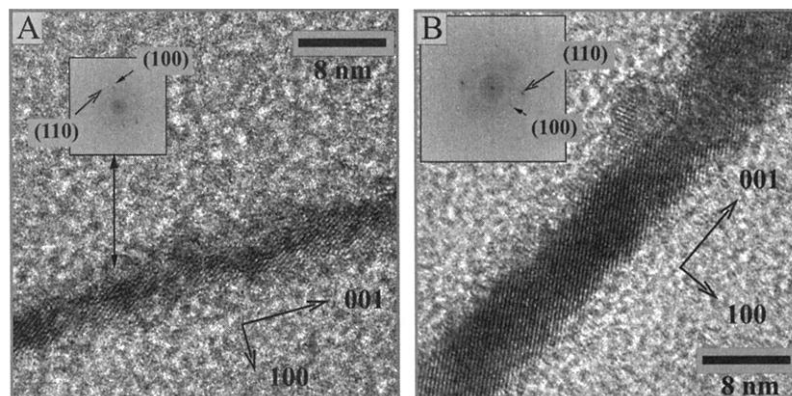


Fig. 3. High-resolution TEM of nanowires made from (A) orange- and (B) red-emitting CdTe quantum dots. The insets show the corresponding diffraction patterns for (001) and (100); vectors of the crystal lattice are indicated by thick arrows. Energy dispersive x-ray spectroscopy showed identical chemical composition in respect to Cd and Te for both nanoparticles and nanowires.

the nanowire formation with a relative luminescence red shift equal to 6 to 8 nm (first 48 hours, red-emitting nanowires) were examined by TEM. In these samples, “pearl-necklace” agglomerates such as the ones presented in Fig. 4A were observed in great abundance. The presence of short nanorods among the “pearl” beads indicates that the nanowires formed not through point-initiated vectorial growth (Fig. 4B) but rather by the recrystallization of multiple nanoparticles in a linear aggregate that fused gradually into one crystal. The similarity of the diameters of nanoparticles and nanowires (Table 1) as well as high monodispersity of the latter substantiates this mechanism. The actual recrystallization may occur via the Ostwald ripening with intermediate Cd^{2+} and Te^{2-} ion transfer from smaller nanoparticles to growing rods in the necklace (4) or as the direct fusion of the particles, as has been demonstrated for Ag rods (13). Although the Ostwald ripening mechanism may seem to be supported by the observed cubic-to-hexagonal phase transition (Fig. 3), the second mechanism appears more probable because of the inherent instability of Te^{2-} and HTe^- in water, which can be easily oxidized by dissolved oxygen (9). The cubic-to-hexagonal phase transition can occur in the entire particle at once (14).

The existence of the pearl-necklace aggregates suggests that understanding the growth

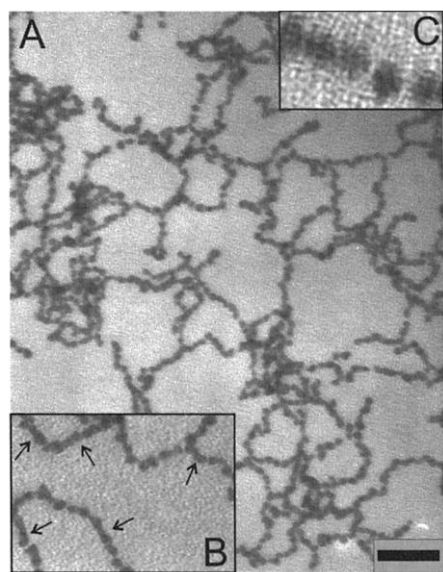


Fig. 4. (A) TEM image of intermediate state of nanoparticle-nanowire transition for 5.4-nm nanoparticles. (B) The enlarged portion of the chain, with short rods marked by arrows. (C) The high-resolution TEM image of the adjacent nanoparticles in the chain. The “pearl-necklace” aggregates were not observed in the standard dispersions of CdTe. TEM samples were prepared on grids with different coatings and with various rinsing and drying procedures to avoid artifacts from evaporation structures.

process depends on an understanding of the collective behavior of nanoparticles and the intermolecular forces between them. The variance of the stabilizer conformations and its distribution over the nanoparticle surface makes short-distance interactions, such as hydrogen bonding of thioglycolic acid headgroups, inefficient for ordering nanoparticles over several hundred nanometers (Fig. 4A). Van der Waals forces between anisotropic semiconductor cores can contribute to unidirectional aggregation of the quantum dot. However, they are quite weak—their energy is estimated to be less than $0.5RT$, which is not enough to stabilize nanoparticle superstructures under ambient conditions (13). The force capable of producing chains of nanocrystals is thus believed to be the dipole-dipole attraction, because it has a long range and is surprisingly strong. The magnitude of the II-VI quantum dot dipoles was experimentally determined to be very high for both hexagonal and cubic nanocrystals, despite the apparent lack of crystal lattice asymmetry of the latter. This effect was attributed to charging chalcogen surface states (15). For CdSe (hexagonal) and ZnSe (cubic) nanocrystals comparable to those used here, the dipole moments were as high as $\mu = 64$ D and 42 D, respectively (15). Though chain formation is well known for magnetic nanoparticles (16), nonmagnetic neutral molecules with high dipole moment also display the same effect in external fields (17). The energy of dipole attraction between nanoparticles can be calculated with the classical formula for aligned dipoles $E = -\mu^2/2\pi\epsilon_0 r(r^2 - d_{NP}^2)$, $\epsilon_0 = 8.85 \times 10^{-12} \text{ C}^2 \text{ J}^{-1} \text{ m}^{-1}$. Estimating the center-to-center interdipolar separation r to be 4.4 nm for nanoparticle diameter $d_{NP} = 3.4$ nm and taking the average value for the dipole moment for the nanoparticle of this size $\mu = 50$ D, the energy of nanoparticle dipole attraction is equal to 8.8 kJ/mole. For nanoparticles with $d_{NP} = 5.6$ nm and $\mu = 98$ D (15), separated by $r = 7.0$ nm (Fig. 4C), this energy can be as high as 10 kJ/mole. Even without additional polarizability terms that should further strengthen the attractive forces, the energy is substantially higher than the energy of regular molecular dipole-dipole attractions (~ 1.5 kJ/mole). The comparison with the molar kinetic energy of linear species $RT = 2.4$ kJ/mole at 25°C clearly

shows the possibility of stable nanoparticle dipole chains in solution.

The pearl-necklace aggregates self-assemble from active nanoparticles obtained after the precipitation of the original stable dispersion with organic solvent. If the methanol precipitation and aqueous redissolution steps were excluded and the original excess thiol stabilizer remained in the solution, nanowires did not form. Therefore, the chain aggregation is initiated by the overall decrease of the stabilizer concentration, which results in the shift of the dynamic equilibrium between nanoparticle-bonded and free stabilizer toward its dissolved state. Furthermore, methanol is a better solvent for thioglycolic acid than water, which also contributes to the shift of the equilibrium. The detachment of mercaptane in the form of R-S^- leads to the decrease of the overall negative charge of the nanoparticles. This reduces the mutual electrostatic repulsion of nanoparticles countering the dipole-dipole attraction. Importantly, the dipole moment is not affected by thinning of the stabilizer coating (15, 18), and therefore the partial stabilizer removal and the increase of the organic content in the media only increases the strength of the dipole-dipole attraction.

Unlike many other nanowires from direct band-gap semiconductors with aspect ratio higher than 10 synthesized in the solution (4, 19, 20), the ones formed here are highly luminescent. CdTe nanowires exhibit luminescence quantum yields, ϕ , as high as 29% for green nanowires ($d_{\text{TEM}} = 2.5$ nm), 16.2% for yellow nanowires ($d_{\text{TEM}} = 3.5$), 6.0% for orange nanowires ($d_{\text{TEM}} = 4.2$), and 2.3% for red nanowires ($d_{\text{TEM}} = 5.6$). These numbers can be compared with the 5 to 10% luminescence quantum yield of CdSe rods with an aspect ratio of 1 to 12, reported previously (12). The high luminescence quantum yields are indicative of the high degree of nanowire crystallinity. The decrease of ϕ for thicker nanowires occurs due to the relaxation of the electron and hole confinement, stimulating the radiative recombination of the exciton in nanostructures of smaller diameter. For all nanowire sizes (Fig. 5), the luminescence was strong enough to observe the emission of single nanowires in a conventional confocal microscopy setup (21). The emission wave-

Table 1. Characteristics of nanowires. The standard deviation was calculated averaging ~ 50 measurements. Asterisk, AFM diameter only.

Nanoparticles		Nanowires			
Luminescence max. (nm)	Diameter (nm)	$d_{\text{TEM}}/d_{\text{AFM}}$ (nm)	SD $\delta_{\text{TEM}}/\delta_{\text{AFM}}$ (%)	Length (nm)	Aspect ratio
520–530	2.5	2.5/2.3	10*	800–1200	320–480
550–565	3.4	3.5/3.1	5/15	1000–1500	300–500
590–605	4.1	4.2/3.7	10*	900–1200	200–300
610–625	5.4	5.6/5.0	5/10	500–1000	100–200

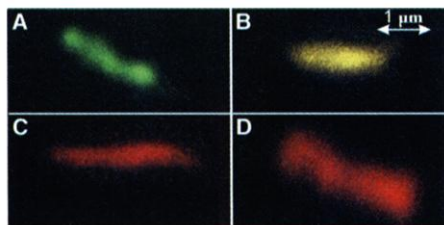


Fig. 5. Confocal microscopy images of individual nanowires with $d_{\text{TEM}} = 2.5$ (A), 3.5 (B), 4.2 (C), 5.6 nm (D) emitting in the green, yellow, orange, and red part of the spectrum, respectively.

length of the nanowire luminescence can be easily tuned by sizing the starting nanoparticles. With respect to the single nanowire luminescence images in Fig. 5, two points should be made: (i) The lengths of the luminescent rods in all images match very well with those seen in AFM and TEM. This means that the entire nanowire is optically active. (Some variation of the emission intensity should be attributed to confocal microscopy optics operating at high magnification.) (ii) The color of the nanowire emission remains the same over its entire length, which is reflective of the constancy of their diameter.

The described synthetic method is very simple and the quality of the produced nanowire is high. They display excellent uniformity in nanowire diameter, have a high aspect ratio, and significant quantum yield. The selection of the original particle sizes offers convenient means for the control of the degree of quantum confinement and nanowire morphology. This synthetic procedure can also be extended to other types of semiconductors: CdSe nanowires of similar dimensions and optical quality were produced in an analogous process (fig. S1), although in smaller yield. Importantly, the described process also exemplifies the ability of the nanoparticles to self-organize into a superstructure due to the intrinsic anisotropy of inter-nanoparticle interactions.

References and Notes

- H. Dai, E. W. Wong, Y. Z. Lu, S. Fan, C. M. Lieber, *Nature* **375**, 769 (1995).
- X. Duan, Y. Huang, Y. Cui, J. Wang, C. M. Lieber, *Nature* **409**, 66 (2001).
- J. D. Holmes, K. P. Johnston, R. C. Doty, B. A. Korgel, *Science* **287**, 1471 (2000).
- B. Gates, Y. Wu, Y. Yin, P. Yang, Y. Xia, *J. Am. Chem. Soc.* **123**, 11500 (2001).
- C. R. Martin, *Science* **266**, 1961 (1994).
- X. Peng et al., *Nature* **404**, 59 (2000).
- S. R. Nicewarner-Pena et al., *Science* **294**, 137 (2001).
- J. S. Yu et al., *Chem. Commun.* 2445 (2000).
- A. L. Rogach et al., *Ber. Bunsen-Ges.* **100**, 1772 (1996).
- A. L. Rogach, D. Nagesha, J. W. Ostrander, M. Giersig, N. A. Kotov, *Chem. Mater.* **12**, 2676 (2000).
- L. S. Li, J. Hu, W. Yang, A. P. Alivisatos, *Nano Lett.* **1**, 349 (2001).
- S. Takeuchi, K. Suzuki, K. Maeda, H. Iwanaga, *Philos. Mag.* **A 50**, 171 (1984).
- B. A. Korgel, D. Fitzmaurice, *Adv. Mater.* **10**, 661 (1998).
- J. N. Wickham, A. B. Herhold, A. P. Alivisatos, *Phys. Rev. Lett.* **84**, 923 (2000).
- M. Shim, P. Guyot-Sionnest, *J. Chem. Phys.* **111**, 6955 (1999).
- S. A. Iakovenko et al., *Adv. Mater.* **11**, 388 (1999).
- A. Peshkovsky, A. E. McDermott, *J. Magn. Reson.* **147**, 104 (2000).
- E. Rabani, B. Hetenyi, B. J. Berne, L. E. Brus, *J. Chem. Phys.* **110**, 5355 (1999).
- Y. Li et al., *Inorg. Chem.* **38**, 1382 (1999).
- Y. Li et al., *J. Am. Chem. Soc.* **123**, 9904 (2001).
- The confocal optical microscopy images were processed by Leica TCS NT confocal microscopy software. 488 nm line of a water-cooled Ar-ion laser was used for luminescence excitation.
- A. A. Mamedov, A. Belov, M. Giersig, N. N. Mamedova, N. A. Kotov, *J. Am. Chem. Soc.* **123**, 7738 (2001).
- N.A.K. thanks the financial support of this project from NSF-CAREER (CHE-9876265), NSF-Biophotonics (BES-0119483), the Air Force Office of Scientific Research (F49620-99-C-0072), OCAST and Nomadics Inc. The authors are grateful to W. Chen for helpful advice and scientific insight. We also appreciate discussions with L. Raff from the Chemistry Department of Oklahoma State University.

Supporting Online Material

www.sciencemag.org/cgi/content/full/297/5579/237/DC1

Fig. S1

Materials and Methods

21 March 2002; accepted 2 May 2002

Role for Stearoyl-CoA Desaturase-1 in Leptin-Mediated Weight Loss

Paul Cohen,¹ Makoto Miyazaki,⁵ Nicholas D. Socci,^{1,2}
 Aaron Hagge-Greenberg,¹ Wolfgang Liedtke,¹
 Alexander A. Soukas,¹ Ratnendra Sharma,¹ Lisa C. Hudgins,³
 James M. Ntambi,^{5,6} Jeffrey M. Friedman^{1,4*}

Leptin elicits a metabolic response that cannot be explained by its anorectic effects alone. To examine the mechanism underlying leptin's metabolic actions, we used transcription profiling to identify leptin-regulated genes in *ob/ob* liver. Leptin was found to specifically repress RNA levels and enzymatic activity of hepatic stearoyl-CoA desaturase-1 (SCD-1), which catalyzes the biosynthesis of monounsaturated fatty acids. Mice lacking SCD-1 were lean and hypermetabolic. *ob/ob* mice with mutations in SCD-1 were significantly less obese than *ob/ob* controls and had markedly increased energy expenditure. *ob/ob* mice with mutations in SCD-1 had histologically normal livers with significantly reduced triglyceride storage and VLDL (very low density lipoprotein) production. These findings suggest that down-regulation of SCD-1 is an important component of leptin's metabolic actions.

Leptin is an adipocyte-derived hormone that regulates energy balance, metabolism, and the neuroendocrine response to altered nutrition (1, 2). The metabolic program that leptin elicits is not explained by its effects on food intake alone (3, 4). Replacing leptin in leptin-deficient (*ob/ob*) mice and humans leads to the depletion of lipid in adipose tissue, liver, and other tissues (5–8). Leptin treatment also improves insulin sensitivity and reduces fat content in lipodystrophic mice and humans (9, 10).

To elucidate the mechanism by which leptin reduces hepatic lipid content, we used microar-

rays to identify genes in liver that were differentially regulated by leptin or by food restriction (pair-feeding). Leptin-treated *ob/ob* mice lose significantly more weight than pair-fed mice, indicating that leptin stimulates energy expenditure [fig. S1 (11)]. Liver RNA from these animals was hybridized to microarrays, and the data were analyzed using a *K*-means clustering algorithm (12). We identified 15 clusters of genes with distinct patterns of expression, six of which correspond to genes specifically regulated by leptin, but not by pair-feeding (fig. S2). To prioritize leptin-regulated genes for functional analysis, we developed an algorithm to identify and rank genes that are specifically repressed by leptin (11). The gene encoding SCD-1 ranked the highest in this analysis (table S1).

The microsomal enzyme SCD-1 is required for the biosynthesis of the monounsaturated fats palmitoleate and oleate from saturated fatty acids (13, 14). SCD-1 RNA levels were highly elevated in untreated *ob/ob* liver (Fig. 1A).

¹Laboratory of Molecular Genetics, ²Center for Studies in Physics and Biology, ³Rogosin Institute, ⁴Howard Hughes Medical Institute, The Rockefeller University, 1230 York Avenue, New York, NY 10021, USA. ⁵Department of Biochemistry and ⁶Department of Nutritional Sciences, University of Wisconsin, Madison, WI 53706, USA.

*To whom correspondence should be addressed. E-mail: friedj@rockvax.rockefeller.edu